Light-Matter Interaction at Surfaces in the Spatiotemporal Limit of Macroscopic Models

M. Lucchini,[1,*] L. Castiglioni,[2] L. Kasmi,[1] P. Kliuiev,[2] A. Ludwig,[1] M. Greif,[2] J. Osterwalder,[2]
M. Hengsberger,[2] L. Gallmann,[1,3] and U. Keller[1]
[1]*Department of Physics, ETH Zurich, 8093 Zürich, Switzerland*
[2]*Department of Physics, University of Zurich, 8057 Zürich, Switzerland*
[3]*Institute of Applied Physics, University of Bern, 3012 Bern, Switzerland*

(Received 2 April 2015; published 22 September 2015)

What is the spatiotemporal limit of a macroscopic model that describes the optoelectronic interaction at the interface between different media? This fundamental question has become relevant for time-dependent photoemission from solid surfaces using probes that resolve attosecond electron dynamics on an atomic length scale. We address this fundamental question by investigating how ultrafast electron screening affects the infrared field distribution for a noble metal such as Cu(111) at the solid-vacuum interface. Attosecond photoemission delay measurements performed at different angles of incidence of the light allow us to study the detailed spatiotemporal dependence of the electromagnetic field distribution. Surprisingly, comparison with Monte Carlo semiclassical calculations reveals that the macroscopic Fresnel equations still properly describe the observed phase of the IR field on the Cu(111) surface on an atomic length and an attosecond time scale.

DOI: 10.1103/PhysRevLett.115.137401　PACS numbers: 78.47.J-, 73.40.-c, 78.68.+m, 79.60.-i

Recent progress in ultrafast measurement techniques has enabled very fundamental studies of charge, energy, and signal transfer with unsurpassed temporal resolution. New insight has been obtained in fundamental light-matter interactions resolving, for example, attosecond (1×10^{-18} s) ionization delays in the gas phase [1–3]. Applying these techniques to solid targets is important for optoelectronics, photovoltaics, and catalysis. More specifically, subfemtosecond electron dynamics in light-matter interactions underline fundamental processes in electronic screening [4–6], collective plasmonic excitations [7,8], interfacial charge transfer [9], and transport [10,11].

Because of the limited photon flux of the attosecond sources, so far experiments have been performed combining attosecond radiation with a phase locked femtosecond infrared (IR) pulse. A proper description of the IR field is thus essential for the correct interpretation of the photoemission dynamics studied with attosecond streaking [12,13] or using the reconstruction of attosecond beating by two-photon transitions (RABBITT [14,15]). In gas phase experiments, the extracted photoemission delays can be written as the sum of three main contributions [16]: the phase of the probe and pump pulses, and an atomic delay. The latter is the quantity of physical interest and can be further decomposed in Wigner delay, related to the ionization via absorption of one XUV photon, and an additional delay induced by the coupling to the probing IR field for both, RABBITT [17] and streaking [18] methods. The absolute phase of the IR field is just an unknown constant and does not carry any sample-specific information. For solid samples, on the other hand, the IR field distribution results from the interaction of the electromagnetic wave with the target, which gives a two-dimensional (2D) transient grating that changes with the direction of incidence on the surface [see Figs. 1(a) and 1(b)]. Thus, in this case the phase of the IR field encoded in an attosecond photoemission experiment can reveal valuable information.

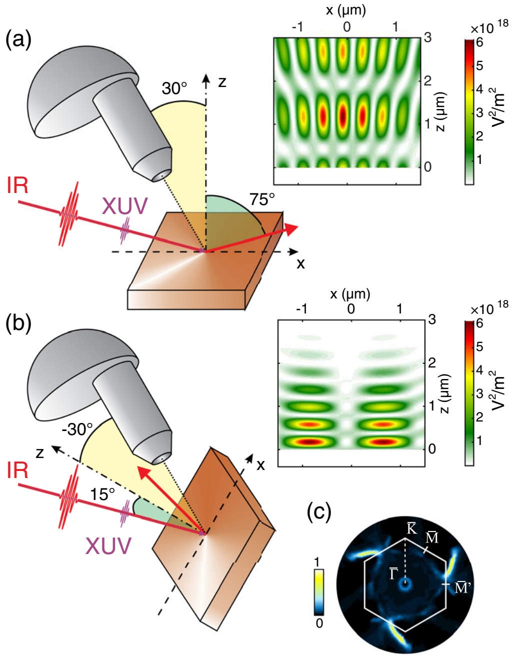

FIG. 1 (color online). Photoemission electron detection geometry using two angles of incidence for the infrared probe field with $\theta_{\mathrm{IR}} = 75°$ (a), and 15° (b). The contour plots show the intensity of the IR transient grating in $\mathrm{V}^2/\mathrm{m}^2$ for the xz plane when the pulse maximum impinges on the surface. (c) Fermi surface map of Cu(111) recorded with He I_α ($h\nu = 21.2$ eV). The white hexagon indicates the borders of the surface Brillouin zone [22].

0031-9007/15/115(13)/137401(5)

This information yields insights into the properties of electron mobility and screening at the interface, such as the electron-scattering rate and memory effects in the optically induced polarization dynamics. Indeed, even if the laser frequency is sufficiently far from the plasma frequency ($\hbar\omega_p \simeq 8.7$ eV for Cu [19]), these effects become important for pulse durations comparable to the electron relaxation time ($\tau_{\mathrm{Cu}} \approx 7$ fs [20]), as is the case for the present work [21]. Under these conditions, transient effects may influence the phase of the reflected field and give a final result that differs from the one predicted by Fresnel. A detailed description of the IR field distribution is therefore not only necessary for a correct interpretation of the photoemission delays, but also essential to access electron transport and screening dynamics, thereby determining where the interaction between photoelectrons and the IR field happens.

At this point it is not clear how macroscopic models, such as the Fresnel equations [23], can be applied in the limit of these length and time scales. Recently photoemission delays in samples with a varying number of Mg adlayers on a W(110) crystal were investigated [24] with the attosecond streaking technique [13]. Starting from the assumption that the Fresnel equations are not valid in this domain, good agreement with theory was achieved with an electric field exponentially damped at the surface. The efficient electron screening was found to reduce the inverse of the exponential decay constant to less than 3 Å, thus making the effect of the electric field inside the solid negligible. By performing attosecond measurements using the RABBITT technique we can show that a description of the vacuum-solid interface in the framework of the Fresnel equations still correctly describes the phase of the reflected IR field for highly reflective metals even on the attosecond time and the atomic length scales probed by the experiment within the experimental error of ≈100 as.

As we recently demonstrated in Ref. [25], RABBITT can also be extended to condensed matter. If compared to streaking, it exhibits several advantages. In particular the required IR intensity is almost a factor 10 lower, thereby reducing the effect of the probe field on the sample and enabling its application even at lower XUV photon energies. Here we investigate the distribution of the IR probe laser field using RABBITT on a Cu(111) surface in a two-target configuration with a gas target reference [25,26].

The adopted setup is described in detail in Ref. [26]. Few-cycle IR pulses with a time duration of 10 fs and energy of ≈300 μJ are generated with a commercial Ti:sapphire laser and additional filament compressor. The pulses are subsequently separated by an 80%:20% beam splitter. The more intense part is focused into a gas cell filled with Ar, where high-order harmonic generation takes place. The weaker part is steered along a delay line before being recombined with the XUV light. Subsequently, both beams are focused by a toroidal mirror into a first interaction region, where a gas nozzle is placed. An additional toroidal mirror placed after the gas target collects the beams and reimages the first focus into a second interaction region where a surface-science end station, equipped with a hemispherical electron analyzer, is installed [22].

Figure 1 displays a schematic of the sample surface orientation. Both XUV and IR pulses are collinearly propagating and p polarized with respect to the surface. The angle between the electron analyzer axis and the incident light is fixed to 45°. The sample is mounted on a 2π goniometer, which allows for accurate control of the orientation. Since the angle between the hemispherical analyzer and the beam path is fixed, changing the angle of incidence θ_{IR} implies an equivalent change of the electron detection angle and, consequently, a different sampling of reciprocal space. As a result band dispersion alone may lead to an angular dependence in the photoemission delays. To minimize band structure effects, we investigated two incidence angles of 15° and 75° that allowed for detection of photoelectrons originating from equivalent regions in momentum space with emission angles of 30° and −30° along the $\overline{\Gamma K}$ direction [see Fig. 1(c)]. We note that a change of the incidence angle rotates the electric field with respect to the crystal orientation. The effect of this on the phase of the matrix elements describing the photoemission process is of the order of a few attoseconds and negligible in comparison to the phase shift of the IR field between the two angular settings.

RABBITT traces obtained for the two different incidence angles are presented in Fig. 2. For each measurement a simultaneous RABBITT in Ne gas [Fig. 2(a)] is performed. This procedure gives a precise and independent calibration of the pump-probe delay, thus allowing for direct comparison of the results obtained at different incidence angles. Discrete peaks corresponding to direct ionization of the $3d$-valence band of Cu by absorption of high-order-harmonic (HH) photons (HH order ranging from 15 to 23) are visible both for $\theta_{\mathrm{IR}} = 75°$ [Fig. 2(b)] and 15° [Fig. 2(c)]. For small values of the pump-probe delay sideband (SB) peaks appear between two consecutive HHs. This signal originates from the interference of two different ionization pathways leading to the same electron final energy and involving absorption of one HH photon plus emission or absorption of an additional IR photon [14,15]. Because of the interference, the SB signal beats with twice the IR carrier frequency ω_{IR} [e.g., see SB 18 in Figs. 2(d)–2(f)]. In the framework of second order perturbation theory, it is possible to show that timing information about the two-color photoionization process is encoded in the phase of the oscillating SB signal [17]. In particular, it can be written as

$$\mathrm{SB}_{2q}(\tau) \propto \cos(2\omega_{\mathrm{IR}}\tau + \Phi_{2q}), \qquad (1)$$

where $2q$ indicates the harmonic order. The experimental values of the SB phases are obtained by bandpass filtering the SB signal and fitting with the function $f(\tau) = e^{-(\tau-a_0)^2/a_1} \cdot a_2 \cos[2\omega_{\mathrm{IR}}(\tau - a_0) + \Phi_{2q}]$ in order to extract Φ_{2q} as a fitting parameter as described in Ref. [25] [see Figs. 2(e) and 2(f)]. For the copper RABBITT trace the phases Φ_{2q} can be divided into four terms: $\Phi_{2q} = \varphi_0 - \Delta\theta_{2q} + 2\varphi_{\mathrm{IR}} - \Delta\varphi_{2q}^{\mathrm{Cu}}$. In the case of Ne, the term

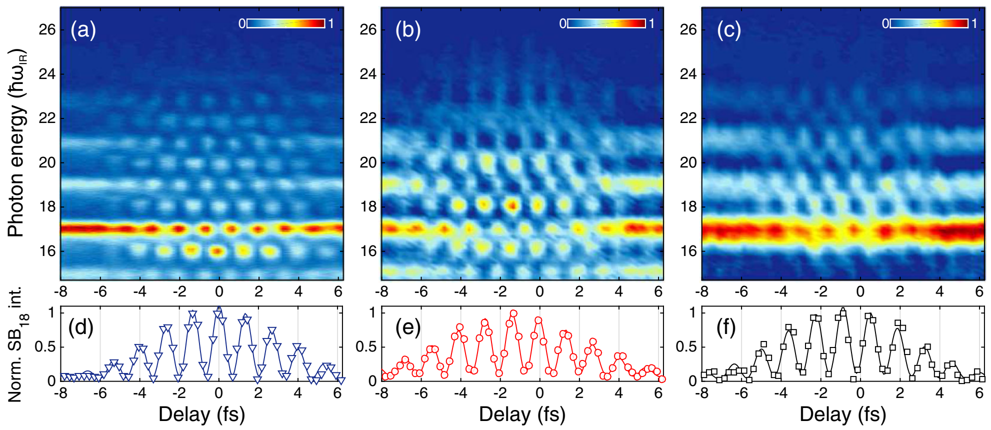

FIG. 2 (color online). Measured RABBITT traces. (a) Example of reference spectrogram in Ne. (b),(c) Typical RABBITT traces obtained with the sample orientations from Figs. 1(a) and 1(b), respectively. A background has been subtracted from the data in (b) and (c) for better visibility of the modulations. (d)–(f) Temporal behavior of $\mathrm{SB}_{18}(\tau)$. Dots represent the experimental data while the solid curves are the result of the fitting function $f(\tau)$ used to extract the phases [25]. A clear phase shift can be observed between (e) and (f).

related to the phase of the IR transient grating $2\varphi_{\mathrm{IR}}$ disappears and the term related to the photoemission delay $\Delta\varphi_{2q}^{\mathrm{Cu}}$ is replaced by the atomic delay $\Delta\varphi_{2q}^{\mathrm{Ne}}$. The other two terms account for the arbitrary choice of the zero in the delay axis φ_0 and the spectral phase of the XUV radiation $\Delta\theta_{2q}$. These terms are identical in both the Ne and Cu measurements and therefore cancel when evaluating the phase difference between the two simultaneous RABBITT traces $\Delta\Phi_{2q} = \Delta\varphi_{2q}^{\mathrm{Cu}} - 2\varphi_{\mathrm{IR}} - \Delta\varphi_{2q}^{\mathrm{Ne}}$. The Ne atomic phase $\Delta\varphi_{2q}^{\mathrm{Ne}}$ is known from theory [27] and can be removed from the experimental data. This allows us to extract the two-color surface-specific ionization phase $\tilde{\varphi}_{2q} = \Delta\varphi_{2q}^{\mathrm{Cu}} - 2\varphi_{\mathrm{IR}}$ on which we will focus hereafter. According to the experimental geometry discussed before, $\Delta\varphi_{2q}^{\mathrm{Cu}}$ does not change significantly with the angle of incidence. Therefore any change in $\tilde{\varphi}_{2q}$ with the IR incidence angle must come from a change in the phase of the IR transient grating φ_{IR}. So the effect of local field distribution is revealed by directly comparing the extracted phases $\tilde{\varphi}_{2q}$ or, equivalently, the delays $\tilde{\tau}_{2q} = \tilde{\varphi}_{2q}/2\omega_{\mathrm{IR}}$.

In order to understand the experimental results and validate our description of the IR field distribution on an attosecond time scale, we performed Monte Carlo (MC) semiclassical calculations using the approach reported in Ref. [28] and including generation of electrons inside the Cu crystal. Assuming single-photon ionization by the XUV as the exciting mechanism, we define the initial time and spectral distribution of the electrons to be replicas of the XUV generating pulses. The probability to detect an unscattered electron excited at the depth z_0 inside the solid is given by the exponential term $P(z_0, E_{\mathrm{kin}}, \theta_{\mathrm{in}}) = \exp\{z_0/[\lambda(E_{\mathrm{kin}})\sin(\theta_{\mathrm{in}})]\}$, where $\lambda(E_{\mathrm{kin}})$ is the

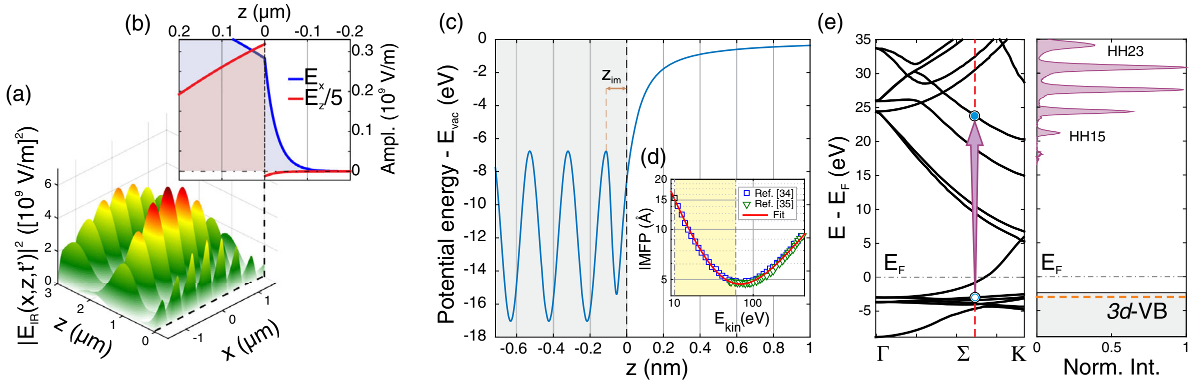

FIG. 3 (color online). (a) Intensity of the 2D-IR grating at the time t' when the center of the pulse reaches the surface for $\theta_{\mathrm{IR}} = 75°$. (b) Corresponding amplitude of the total IR field along the normal direction z at $x = 0$. The blue and red curves show x and z components, respectively. The z component is divided by 5 for a better comparison. The IR pulse has a center wavelength of 786 nm, Gaussian temporal and spatial envelopes define a time duration of 10 fs and lateral dimension of 70 μm. The intensity is set to 5×10^{11} W/cm^2 in order to match the experimental conditions. (c) Model potential according to Ref. [29]. The image plane is located at $z = 0$, at a distance z_{im} from the center of the top atomic layer. (d) Inelastic mean free path (IMFP), squares and triangles are data from Refs. [34] and [35], solid red line is the parametrized curve used in the calculations. The yellow shaded area marks the energy region under investigation. (e) Schematic of the XUV photoionization of the 3d-valence band of Cu. Left panel, band structure [33]; right panel, HH photon spectrum.

energy-dependent inelastic mean free path (IMFP) [Fig. 3(d)], θ_{in} is the angle between the surface normal and the initial direction of the electron, and E_{kin} is the electron kinetic energy in the solid. The potential inside the solid [Fig. 3(c)] is described with the effective single-active electron potential proposed by Chulkov and co-workers [29] for the valence band of Cu(111). In such a potential we locate the image-plane at $z_{\text{im}} = 1.12$ Å from the center of the top atomic layer [30]. The final energy of the electrons reaching the detector is calculated using the classical equations of motion for a charged particle in an electric field. Since no narrow-band resonances which could render the simple group delay picture meaningless [31] are involved in the photoionization process, ballistic transport is expected to correctly describe the observed relative attosecond photoemission delays [30]. The total IR electric field $E_{\text{IR}}(x,z,t)$ is obtained using the Fresnel equations [32] in the slowly varying envelope approximation [28] [see Figs. 3(a)–3(b) for the case of $\theta_{\text{IR}} = 75°$]. For $z < 0$ the amplitude of the evanescent wave decays exponentially with a skin depth $\delta_{\text{IR}} \approx 25$ nm after an initial sharp drop at the surface directly following from the conservation of the z component of the displacement vector [Fig. 3(b)]. Inside the Cu crystal the free-electron approximation is justified by the parabolic dispersion of the Cu band structure [33] [Fig. 3(e)] probed in the experiment. The quantum phase acquired by the electrons during their motion is then estimated with the Volkov phase. Finally, RABBITT traces are calculated performing a coherent sum over the electrons that reach the detector after the interaction with the 2D-IR grating [28]. The theoretical phases $\tilde{\varphi}_{2q}$ can then be extracted from the calculated spectrograms following the same procedure applied to the experimental data.

Since the Fresnel equations are based on the macroscopic response of the material they are, in general, not expected to hold when microscopic properties of the metal-vacuum interface are probed on the attosecond time scale. In particular, they predict a discontinuous normal component of the electric field [red curve in Fig. 3(b)], associated with an unrealistic electron density profile at the interface [23]. In the case of copper, however, the real part of the index of refraction is < 1 within the spectral range covered by the IR pulse [36]. Thus, following the Fresnel laws, total reflection and a strongly damped evanescent wave inside the crystal are expected. For this reason, even if they predict a longer skin depth ($\delta_{\text{IR}} \approx 25$ nm) than the one suggested by the model presented in Ref. [24], the Fresnel equations finally lead to the same result: the sudden drop of field strength at the interface makes the IR wave in the solid too weak to have an influence on the photoemission process.

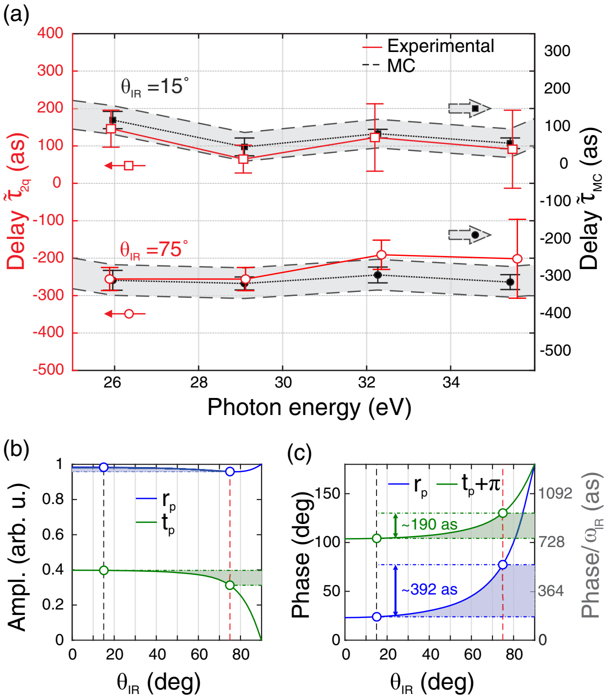

FIG. 4 (color online). (a) Surface-specific two-color photoemission delays $\tilde{\tau}_{2q}$ for two incidence angles $\theta_{IR} = 15°$ (red open squares) and 75° (red open circles) and the results of semiclassical Monte Carlo calculations $\tilde{\tau}_{\text{MC}}$ (black solid symbols). The sum of the error bars representing the confidence interval associated to the fitting procedure applied to extract $\tilde{\tau}_{\text{MC}}$ and the uncertainty in the gas phase reference measurement used for time delay calibration, is plotted as a shaded area around the theoretical predictions. (b), (c), Amplitude and phase of the reflection (r_p in blue) and transmission (t_p in green) coefficients calculated using Fresnel equations.

Figure 4 shows the experimental and simulated delays $\tilde{\tau}_{2q}$ for the two sample orientations. The error bars indicate the statistical standard deviation calculated over an ensemble of 13 measurements for both orientations. As one can see, a clear effect of the sample orientation is detected. Indeed, photoemission at $\theta_{\text{in}} = 15°$ is delayed on average by $\langle \tilde{\tau}_{2q}^{15°} - \tilde{\tau}_{2q}^{75°} \rangle = 332 \pm 96$ as with respect to $\theta_{\text{in}} = 75°$. This difference is well reproduced by the results of our MC calculations, obtained launching 10^6 electrons for every pump-probe delay step. The agreement between experiment (red-solid curve) and Fresnel-based theory (black-dotted curve) in Fig. 4(a) indicates the validity of the Fresnel picture on the microscopic and attosecond spatiotemporal scales. A closer look at the angular dependence of the reflection coefficient r_p calculated with the Fresnel equations for p-polarized light reveals the physical origin of the observed relative delay. While the amplitude of r_p [blue curve in Fig. 4(b)] does not vary substantially with the incidence angle θ_{IR}, the phase of r_p [Fig. 4(c)] changes by 54°, which corresponds to a delay of ≈392 as at the IR angular frequency, in good agreement with the measured shift $\langle \tilde{\tau}_{2q}^{15°} - \tilde{\tau}_{2q}^{75°} \rangle$. Note that an increasing IR phase corresponds to a more delayed IR pulse, which results in the SB oscillation to be advanced in delay and therefore a decreasing $\tilde{\tau}_{2q}$. This fact explains the change of sign between the experimental observations and the phase of the reflection coefficient r_p. We observe a constant offset of about 50 as between calculation and experiment. This offset could be addressed by a more detailed description of the absolute photoemission delays, which is beyond the scope of the present work and will require better accuracy in future measurements.

In conclusion, we used RABBITT traces with a common Ne reference to investigate the angular dependence of the measured photoelectron phase on the 2D transient grating created upon reflection of the IR probe field at the surface of a Cu(111) crystal. Experimental data acquired close to normal or grazing incidence show a clear shift of the two-color photoemission delay, which is directly related to the different phases of the IR transient grating. Semiclassical calculations based on ballistic transport of the electrons and Fresnel equations reproduce the experimental data within the measurement error of around 100 as and fully explain the origin of the observed angle-dependent difference in photoemission delay. We conclude that (i) despite being derived from macroscopic considerations, the Fresnel equations correctly describe the phase of the IR field at the surface also on microscopic and attosecond scales; (ii) since the phases of the reflected and evanescent wave change differently with the incidence angle [see Fig. 4(c)], efficient and fast electron screening has to occur at the interface in order to render the influence of the evanescent wave negligible. We expect that for a target with lower reflection coefficient, the experiment is more sensitive to the phase of the transmitted field. This would let us investigate the validity of the Fresnel equations inside the solid and study the change in the normal component of the electric field across a finite vacuum-solid interface on microscopic length scales.

This research was supported by the NCCR MUST, funded by the Swiss National Science Foundation, and an ETH Zurich postdoctoral fellowship.

---

[*] mlucchini@phys.ethz.ch

[1] M. Schultze *et al.*, Science **328**, 1658 (2010).

[2] K. Klünder, J. M. Dahlström, M. Gisselbrecht, T. Fordell, M. Swoboda, D. Guénot, P. Johnsson, J. Caillat, J. Mauritsson, A. Maquet, R. Taïeb, and A. L'Huillier, Phys. Rev. Lett. **106**, 143002 (2011).

[3] P. Eckle, A. N. Pfeiffer, C. Cirelli, A. Staudte, R. Dörner, H. G. Muller, M. Büttiker, and U. Keller, Science **322**, 1525 (2008).

[4] A. Borisov, D. Sánchez-Portal, R. D. Muiño, and P. Echenique, Chem. Phys. Lett. **387**, 95 (2004).

[5] A. K. Kazansky and P. M. Echenique, Phys. Rev. Lett. **102**, 177401 (2009).

[6] C.-H. Zhang and U. Thumm, Phys. Rev. Lett. **102**, 123601 (2009).

[7] A. K. Kazansky and P. M. Echenique, Phys. Rev. B **81**, 193413 (2010).

[8] C.-H. Zhang and U. Thumm, Phys. Rev. A **84**, 063403 (2011).

[9] A. Föhlisch, P. Feulner, F. Hennies, A. Fink, D. Menzel, D. Sanchez-Poral, P. M. Echenique, and W. Wurth, Nature (London) **436**, 373 (2005).

[10] A. Cavalieri, N. Muller, T. Uphues, V. Yakovlev, A. Baltuska, B. Horvath, B. Schmidt, L. Blumel, R. Holzwarth, S. Hendel, M. Drescher, U. Kleineberg, P. Echenique, R. Kienberger, F. Krausz, and U. Heinzmann, Nature (London) **449**, 1029 (2007).

[11] S. Neppl, R. Ernstorfer, E. M. Bothschafter, A. L. Cavalieri, D. Menzel, J. V. Barth, F. Krausz, R. Kienberger, and P. Feulner, Phys. Rev. Lett. **109**, 087401 (2012).

[12] J. Itatani, F. Quéré, G. L. Yudin, M. Y. Ivanov, F. Krausz, and P. B. Corkum, Phys. Rev. Lett. **88**, 173903 (2002).

[13] Y. Mairesse and F. Quéré, Phys. Rev. A **71**, 011401 (2005).

[14] P. Paul, E. Toma, P. Breger, G. Mullot, F. Augé, P. Balcou, H. Muller, and P. Agostini, Science **292**, 1689 (2001).

[15] H. Muller, Appl. Phys. B **74**, s17 (2002).

[16] Y. Mairesse, A. de Bohan, L. J. Frasinski, H. Merdji, L. C. Dinu, P. Monchicourt, P. Breger, M. Kovačev, R. Taïeb, B. Carré, H. G. Muller, P. Agostini, and P. Saliéres, Science **302**, 1540 (2003).

[17] J. M. Dahlström, A. L'Huillier, and A. Maquet, J. Phys. B **45**, 183001 (2012).

[18] R. Pazourek, S. Nagel, and J. Burgdörfer, Faraday Discuss. **163**, 353 (2013).

[19] E. J. Zeman and G. C. Schatz, J. Phys. Chem. **91**, 634 (1987).

[20] P. B. Johnson and R. W. Christy, Phys. Rev. B **6**, 4370 (1972).

[21] U. Bovensiepen, S. Declair, M. Lisowski, P. A. Loukakos, A. Hotzel, M. Richter, A. Knorr, and M. Wolf, Phys. Rev. B **79**, 045415 (2009).

[22] M. Greif, L. Castiglioni, D. Becker-Koch, J. Osterwalder, and M. Hengsberger, J. Electron Spectrosc. Relat. Phenom. **197**, 30 (2014).

[23] A. Georges, Opt. Commun. **188**, 321 (2001).

[24] S. Neppl, R. Ernstorfer, A. L. Cavalieri, C. Lemmel, G. Watcher, E. Magerl, E. M. Bothschafter, M. Jobst, M. Hofstetter, U. Kleineberg, J. V. Barth, D. Menzel, J. Burgdörfer, P. Feulner, F. Krausz, and R. Kienberger, Nature (London) **517**, 342 (2015).

[25] R. Locher, L. Castiglioni, M. Lucchini, M. Greif, L. Gallmann, J. Osterwalder, M. Hengsberger, and U. Keller, Optica **2**, 405 (2015).

[26] R. Locher, M. Lucchini, J. Herrmann, M. Sabbar, M. Weger, A. Ludwig, L. Castiglioni, M. Greif, M. Hengsberger, L. Gallmann, and U. Keller, Rev. Sci. Instrum. **85**, 013113 (2014).

[27] J. Mauritsson, M. B. Gaarde, and K. J. Schafer, Phys. Rev. A **72**, 013401 (2005).

[28] M. Lucchini, A. Ludwig, L. Kasmi, L. Gallmann, and U. Keller, Opt. Express **23**, 8867 (2015).

[29] E. Chulkov, V. Silkin, and P. Echenique, Surf. Sci. **437**, 330 (1999).

[30] Q. Liao and U. Thumm, Phys. Rev. A **89**, 033849 (2014).

[31] M. Sabbar, S. Heuser, R. Boge, M. Lucchini, T. Carette, E. Lindroth, L. Gallmann, C. Cirelli, and U. Keller, Phys. Rev. Lett. **115**, LB14900 (2015).

[32] K. Kliewer, Surf. Sci. **101**, 57 (1980).

[33] V. N. Strocov, R. Claessen, G. Nicolay, S. Hüfner, A. Kimura, A. Harasawa, S. Shin, A. Kakizaki, P. O. Nilsson, H. I. Starnberg, and P. Blaha, Phys. Rev. Lett. **81**, 4943 (1998).

[34] S. Tanuma, C. J. Powell, and D. R. Penn, Surf. Interface Anal. **43**, 689 (2011).

[35] S. Tanuma, C. J. Powell, and D. R. Penn, Surf. Interface Anal. **17**, 911 (1991).

[36] A. D. Rakić, A. B. Djurišić, J. M. Elazar, and M. L. Majewski, Appl. Opt. **37**, 5271 (1998).